Received: 20 January 2023 | Revised: 8 June 2023 | Accepted: 11 June 2023

DOI: 10.1111/bre.12802

RESEARCH ARTICLE

Basin Research IAS EAGE WILEY

How post-salt sediment flux and progradation rate influence salt tectonics on rifted margins: Insights from geodynamic modelling

Leonardo M. Pichel[1] | **Ritske S. Huismans**[1] | **Robert Gawthorpe**[1] | **Jan Inge Faleide**[2]

[1]Department of Earth Science, University of Bergen, Bergen, Norway

[2]Department of Geosciences, University of Oslo, Oslo, Norway

Correspondence
Leonardo M. Pichel, Department of Earth Science, University of Bergen, Bergen, Norway.
Email: leonardo.m.pichel@uib.no

Funding information
UiB-Equinor Akademia

Abstract

Continental rifted margins can be associated with widespread and thick salt deposits, which are often formed during the final stages of rifting, prior to breakup. These salt-bearing margins are typically characterized by pronounced post-rift salt tectonics with variable and complex structural styles and evolution. We use a lithosphere-scale geodynamic numerical model to investigate the role of varying post-rift sediment fluxes and progradation rates on rifted margin salt tectonics. We focus on a single, intermediate, rifted margin type and salt basin geometry to explore scenarios with different: (i) constant and (ii) time-varying post-salt sediment fluxes. We demonstrate that these promote significant contrasts in the style and magnitude of salt tectonics in the proximal, transitional and distal margin domains. The differences are primarily controlled by the relationship between the rates of sediment progradation (V_{prog}) and salt flow (V_s). When $V_{prog} > V_s$, the salt is rapidly buried and both vertical and lateral salt flow are suppressed across the entire margin. When $V_{prog} < V_s$, the salt flows vertically and seaward faster than sediments prograde producing major diapirism in the proximal domain and major distal nappe advance, but only moderate overburden extension and distal diapirism. When $V_{prog} \sim V_s$, there is moderate proximal diapirism and distal nappe advance, but major updip extension and downdip shortening, which produces major distal diapirism. Modelling results are comparable to various natural systems and help improve our understanding of the controls and dynamics of salt tectonics along salt-bearing rifted margins.

KEYWORDS

numerical modelling, progradation, rifted margins, salt tectonics, sediment loading

1 | INTRODUCTION

Thick salt deposits are found in various rifted margins worldwide, often referred to as salt giants, and are commonly associated with significant salt tectonics and complex structural styles (Davison et al., 2012; Jackson & Hudec, 2017; Kukla et al., 2018; Rowan, 2014, 2020). The majority and largest rifted margin salt basins are formed

during the latest stages of rifting (i.e. late syn-rift), shortly before continental break-up (Hudec & Jackson, 2007; Lentini et al., 2010; Rowan, 2014, 2020). These salt basins can be associated with different styles of rift-related crustal architecture and margin width (Pichel et al., 2022b) and post-rift sediment fluxes (Davison et al., 2012; Kukla et al., 2018; Lentini et al., 2010). Examples include the Gulf of Mexico (Hudec et al., 2013; Hudec & Norton, 2019; Peel et al., 1995), Brazil (Davison et al., 2012; do Amarante et al., 2021; Pichel et al., 2018, 2020), West Africa (Epin et al., 2021; Hudec & Jackson, 2004; Jackson et al., 2008; Marton et al., 2000), the Red Sea (Mohriak & Leroy, 2013; Rowan, 2014), NW Africa (Pichel et al., 2019; Tari et al., 2003, 2017; Uranga et al., 2022) and Nova Scotia (Albertz et al., 2010; Deptuck & Kendell, 2017; Figure 1a).

Few studies have attempted to correlate crustal architecture with post-rift salt tectonics at a regional scale along rifted margins (cf., Epin et al., 2021; Kukla et al., 2018; Pichel et al., 2021; Quirk et al., 2012; Rowan, 2014, 2020), and even fewer have attempted to model it (Allen & Beaumont, 2016; Allen et al., 2020; Goteti et al., 2013; Pichel et al., 2022a, 2022b). In a recent study (Pichel et al., 2022b), we used a geodynamic modelling approach to investigate the interplay between crustal-scale rifted margin architecture with late syn-rift salt deposition and post-rift salt tectonics for various margin types (Figure 1). We expand on this previous work here by applying the same forward numerical modelling approach to investigate the influence of post-rift (i.e. post-salt) sediment flux and the associated progradation rate on rifted margin salt tectonics for a single margin type. This approach does not prescribe the geometries of the lithosphere and the salt basins and incorporates a more realistic simulation of post-rift sedimentation using a dynamically evolving depositional profile. (cf. Pichel et al., 2022b).

We test two types of post-salt sediment fluxes: (a) constant and (b) time-varying. We apply these scenarios for a salt-bearing rifted margin of intermediate width of ca. 150 km. The aim of our study was to investigate how varying post-salt sedimentation controls: (1) the relative contributions between different structural processes (i.e. seaward salt flow, diapirism, updip extension, downdip shortening and nappe advance), on regional salt tectonics, and (2) the variation on the style of salt diapirism and minibasin formation across rifted margins (Figure 1b). Our modelling results are comparable to several rifted margin salt basins, in particular to segments of the Nova Scotia and NW Africa margin, the Espirito Santo and Campos margins in Brazil, Benguela in West Africa and the southern Gulf of Mexico.

Highlights

- We test the effects of different post-salt sediment fluxes on rifted margin salt tectonics.
- Significant contrasts are controlled by the ratio between the rates of progradation (V_{prog}) and salt flow (V_s).
- The effects of the V_{prog}/V_s ratio vary according to different margin domains, from proximal, intermediate to distal.

2 | NUMERICAL MODELLING APPROACH AND DESIGN

We use an arbitrary Lagrangian–Eulerian (ALE) finite element method for the solution of thermo-mechanical coupled, plane strain, incompressible viscous-plastic creeping (Stokes) flows (Erdős et al., 2014; Theunissen & Huismans, 2019; Thieulot, 2011). The model solves the quasi-static force balance equations for incompressible creeping flows in two dimensions coupled with the time-dependent heat conservation equation. The reader is referred to Theunissen and Huismans (2019) and Pichel

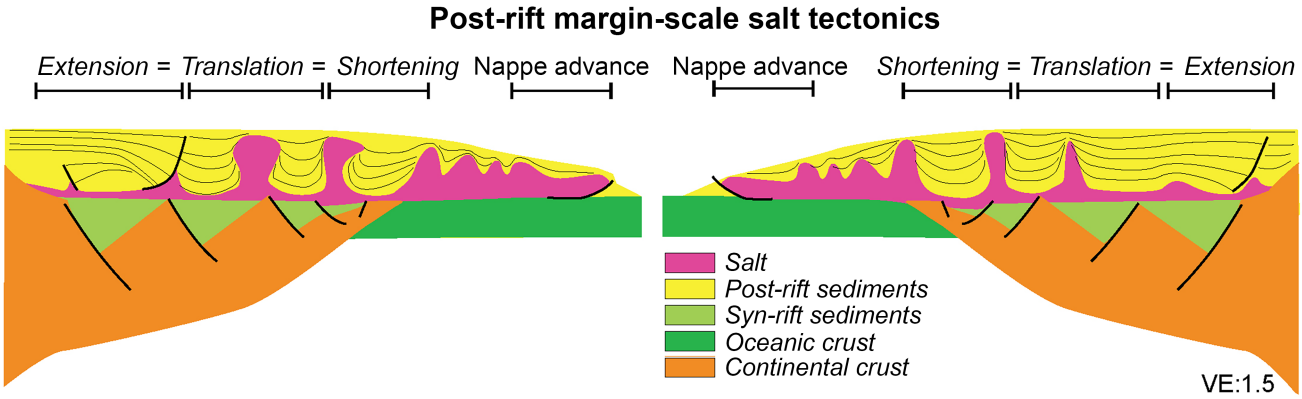

FIGURE 1 Synoptic diagram of regional post-rift salt tectonics along rifted passive margins with late syn-rift salt deposition (adapted from Pichel et al., 2022a).

et al. (2022a, 2022b), for a more complete description of the governing equations and thermal boundary conditions. A list of material parameters is given in Table 1.

2.1 | Model set-up

The models present an idealized rheologically layered lithosphere above a sublithospheric mantle in a 600 km high and 1200 km wide model domain (Figure 2). The lithosphere consists of a 35 km thick crust and a 90 km mantle lithosphere overlying sublithospheric mantle. The Eulerian grid consists of 2400 and 290 elements in the horizontal and vertical directions respectively. The distribution of the elements is irregular in the vertical direction allowing a higher resolution ($\Delta z = 200$ m) in the upper crust and ($\Delta z = 100$ m) in syn- to post-rift sediments (first 20 km), the focus of this study. The resolution in the

TABLE 1 Parameters for the lithosphere-scale thermo-mechanical models of intermediate width salt-bearing rifted margins used in the study.

Parameters	Symbol	Units	Salt	Sediments	Upper crust (0–25 km)	Lower crust (25–35 km)	Lithospheric mantle	Sub-lithospheric mantle
Rheological parameters								
Effective viscosity range	μ_{eff}	Pa.s	5×10^{18}	10^{18}–10^{27}	10^{18}–10^{27}	10^{18}–10^{27}	10^{18}–10^{27}	10^{18}–10^{27}
Angle of internal friction	ϕ_{eff}	—	—	15	15		15	
→ after strain weakening	ϕ_{eff}	—	—	2	2		4	
Initial cohesion	C	MPa	—	10	20		20	
→ after strain weakening	C	MPa	—	4	4		20	
Strain weakening range	—	—	—	0.05–1.05				
Flow law	—	—	—	WQtz[a]			WO[b]	
Scaling factor	f_c	—	—	1	1		5	1
Power law exponent	n	—	—	4	4		3	
Activation energy	Q	kJ/mol	—	222.81	222.81		429.83	
Constant	A	Pa^{-n}/s	—	8.574×10^{-28}			1.758×10^{-14}	
Activation volume	V	m^3/mol	—	0.0			15×10^{-6}	
Density at $T_0 = 273$ K	ρ_0	kg/m^3	2200	2400	2750	2900	3300	
Thermal parameters								
Thermal conductivity	k	W/m/K	2.25				2.25–5.6	
							2.25–51.46	
Heat capacity	c_p	J/K/kg	803.57		818.18	775.86	681.81	
Thermal diffusivity	κ	m^2/s	1.0×10^{-6}				$1–2.5\times10^{-6}$	
							$1–22.87\times10^{-6}$	
Heat production rate	H	W/m	0.8×10^{-6}		1.12×10^{-6}	0.48×10^{-6}	0	
Thermal expansion	α_T	1/K	3×10^{-5}	3.1×10^{-5}				
Boundary conditions								
Surface temperature	T_{surf}	°C	0					
Pre-rift sediment thickness	$h_{pre\text{-}sed}$	km	3					
Initial Moho depth	d_{moho}	km	35					
Moho temperature	T_{moho}	°C	550					
LAB depth	d_{LAB}	km	125					
LAB temperature	T_{LAB}	°C	1328					
Basal temperature	T_{LM}	°C	1520					
Extension velocity	V_{ext}	cm/year	1					

Note: Flow laws are based on power law with creep parameters from wet quartz (Gleason & Tullis, 1995) and wet olivine (Karato & Wu, 1993). Values are given with two digits precision.

Abbreviations: LAB, Lithosphere-Asthenosphere Boundary; WO, wet olivine; WQtz, wet quartz.

[a]Dislocation creep models for WQtz.

[b]Dislocation creep models for WO.

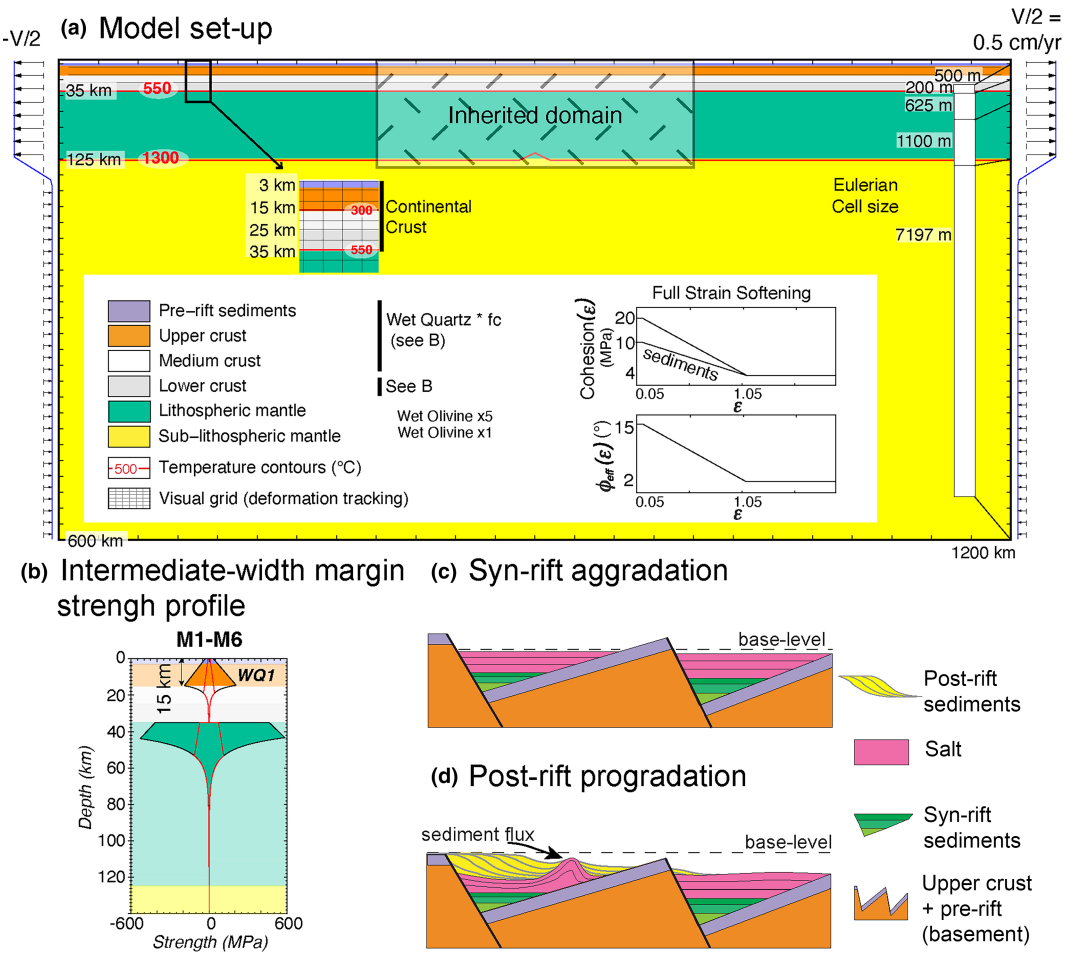

FIGURE 2 (a) Model set-up showing the rheologically-layered structure, boundary conditions, initial thermal state and frictional-plastic strain softening conditions (adapted from Pichel et al., 2022a). The parameters used are listed in Table 1. (b) Lithosphere strength profile of intermediate margin types with a scaling factor (f_c) WQ = 1 used in this study. (c) Schematic diagram illustrating syn-rift aggradation for pre- and salt sediments in which sediments aggrade towards local basement minima. (d) Schematic diagram illustrating post-rift (post-salt) dynamic progradation in which the depositional profile changes in shape through time according to the evolving underlying salt topography.

horizontal direction is 500 m for the entire model domain. Extensional horizontal velocity boundary conditions ($v = \pm 0.5$ cm/year) are applied to the lithosphere, and the corresponding exit flux is balanced by a low-velocity inflow in the sublithospheric mantle. The top of the model is a free surface. The sides and base are vertical and horizontal free-slip boundaries respectively (Figure 2a).

The crust follows a wet quartz rheology (WQ) (Gleason & Tullis, 1995) with a scaling factor (f_c) of 1, representative of intermediate-strength crustal types (Figure 2b) (cf. Theunissen & Huismans, 2019). The salt is treated as a linear viscous material with an intermediate salt viscosity of 5×10^{18} Pa s and a density of 2200 kg/m^3 (cf. Pichel et al., 2022a, 2022b). Syn- and post-rift sediments have an average density of 2400 kg/m^3. We do not incorporate compaction in our models for simplification purposes, but we include a supplementary set of models testing different post-salt sediment densities: Supplementary model SM7 with post-salt sediment density equal to the salt (2200 kg/m^3) and SM8 with post-salt sediment density only very slightly higher than the salt (2300 kg/m^3; Figure S1).

2.2 | Sedimentation

Sedimentation occurs by filling all accommodation space between the model surface and a defined base(sea)-level with sediments at each time step. We use aggradation for syn-rift clastics and salt (Figure 2c), and progradation for the post-rift (post-salt) sediments (Figure 2d; see Pichel et al., 2022a, 2022b). Aggradation is controlled by a horizontal bathymetric profile with a vertical position (i.e. base-level) that is adjusted for each main depositional stage, that is, syn-rift clastics and salt deposition (Figure 2c). For the post-rift (i.e. post-salt) progradation, we use a dynamic depositional profile where sediment deposition and progradation rate are controlled by the sediment flux, Q_s (e.g. Pichel et al., 2022a, 2022b; Theunissen &

Huismans, 2019) into the basin (Figure 2c). This allows for a more self-consistent evolution of the post-salt sequences relative to previous modelling studies which prescribed a constant, albeit moving Half-Gaussian depositional profile (cf. Allen & Beaumont, 2016; Gemmer et al., 2004; Goteti et al., 2013).

All models include water load and syn-rift pre-salt aggradation at 25 m/Myr at a −1 km base-level. This is followed by fast salt aggradation at 2 km/Myr at −750 m of base-level during the last stages (ca. 2 Myr) of rifting, salt is thus deposited rapidly after most of crustal extension and immediately prior to continental break-up (cf., Pichel et al., 2022a). This relative timing of salt deposition and the sediment fluxes for both salt and pre-salt sequences are consistent with various studies of passive margin late syn-rift salt basins (cf., Davison et al., 2012; Hudec et al., 2013; Kukla et al., 2018; Lentini et al., 2010; Mohriak & Leroy, 2013; Rowan, 2014, 2020; Tari et al., 2017). Post-rift dynamic progradation occurs at −250 m of base-level and with variable sediment flux.

2.3 | Model design

The study comprises two sets of models. In the first, we explore the effects of three different, albeit constant post-salt sediment fluxes: 1×10^{-3}, 5×10^{-4} and 2.5×10^{-4} m^2/s (ca. 30, 15 and 7.5 km^2/Myr respectively) and correspond to high (M2), medium (M1, reference model) and low (M3) sediment fluxes respectively. In the second set, we use time-variable sediment flux to reproduce more common rifted margin scenarios where post-breakup sedimentation fluxes vary through time by commonly decreasing gradually or with relatively early and short-lived pulses of increased flux (cf., Baby et al., 2020). We test two cases with a sediment flux pulse centred on 20 Myr and lasting 10 Myr (early post-break-up) against a constant background sediment flux (M4 and M5), and one scenario (M6) with a decrease in sediment flux during the first 5 Ma following continental break-up followed by constant low sediment flux (Figure 3). M4 and M5 have the same peak sediment flux (30 km^2/Myr) at 20 Myr but have different background sediment fluxes. M4 has a low background sediment flux (7.5 km^2/Myr), whereas M5 has a medium background sediment flux (15 km^2/Myr). In Model M6, the sediment flux gradually decrease from a high (30 km^2/Myr) to a low (7.5 km^2/Myr) sediment flux immediately after continental breakup and salt deposition, between 13 and 18 Myr. The range of sediment flux values used is consistent with post-rift sediment fluxes that range from 0.3 to 52 km^2/Myr along the South Atlantic African margins (cf. Baby et al., 2020).

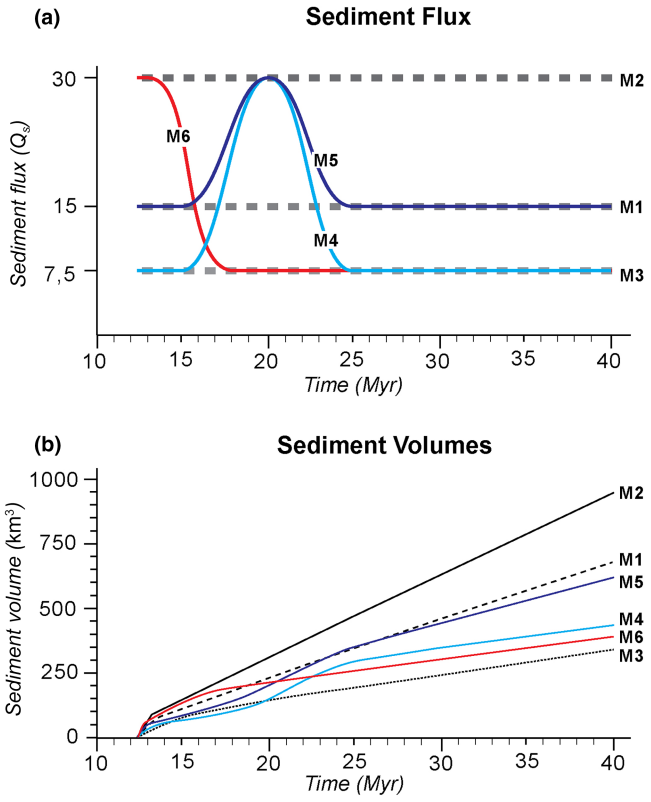

FIGURE 3 (a) Sediment flux variations through time and (b) sediment volumes and for the models of intermediate-width margin.

3 | RESULTS

We first present the initial, pre-breakup salt basin geometries for both conjugate margins and the time evolution of the reference model M1, which has a medium sediment flux. We then describe and compare the final stages of the other models with different sediment fluxes. We describe only the left margin of each model as the width and geometry of their conjugates and the overall style of salt tectonics are similar. Animations of all models (both left and right margins) are presented in the supplementary material.

3.1 | Medium constant sediment flux model M1

Reference model M1 shows rifting of an intermediate-strength crust with the development of broadly symmetric conjugate margins of similar width (ca. 150 km) and small differences in syn-rift fault and crustal geometries (Figure 4a). Breakup is achieved between 12.4 and 13 Myr, immediately after the end of salt deposition (12.4 Myr). The left margin comprises ca. 5–30 km wide grabens and half-grabens bounded by predominantly seaward-dipping normal faults that cut the entire upper crust and detach

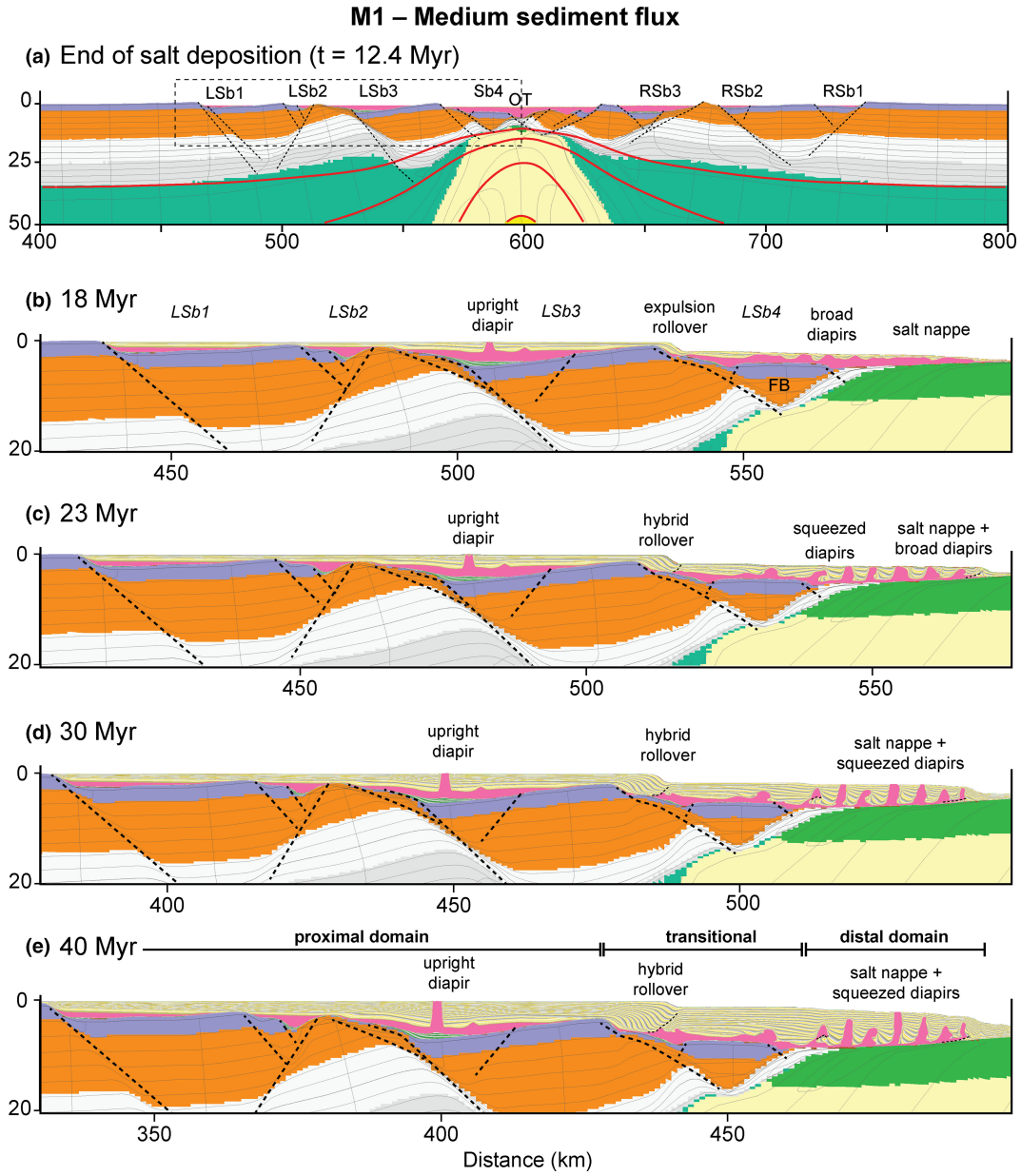

FIGURE 4 (a) Conjugate margins at the end of the salt deposition, immediately prior to continental breakup showing the initial salt basin geometries for the intermediate-width margin type. Multi-stage evolution of reference intermediate-width margin model (M1—left margin) with medium post-rift sediment flux (ca. 15 km^3/Myr): (b) 18 Myr, (c) 23 Myr, (d) 30 Myr and (e) 40 Myr. Faults in black dashed lines. The numbered LSb and RSb refer to left- and right-margin salt sub-basins respectively.

at the weaker lower crust (Figure 4a). The faults and pre-salt syn-rift strata become younger seaward so that the most distal grabens have little to no pre-salt sediment (Figure 4). The width of the grabens also decreases seaward as the crust is gradually thinned in this direction (Figure 4a).

The syn-rift grabens control the geometry, width and thickness of overlying salt sub-basins (LSb1-4), with the salt being thickest (up to 4 km) in their hanging walls and thinning on to footwall highs and horsts (Figure 4a). The two most proximal grabens form narrow (ca. 5–20 km wide) and thin (0.6–1 km thick) sub-basins (LSb1 and LSb2). The intermediate sub-basin (LSb3) has a maximum salt thickness of 1.6 km and is ca. 34 km wide (Figure 4a). These three proximal sub-basins (LSb1-3) are disconnected from each other. The distal salt sub-basin (LSb4) is the thickest, with salt varying from 1.5 km over the distal fault block (FB, Figure 4a) to ca. 4 km thick in the outer trough (OT, Figure 4a). The initially thickest salt in the OT is thinned and stretched shortly after its deposition as the two conjugate margins and their respective salt basins separate (cf. Pichel et al., 2022a).

By 18 Myr of model evolution, ca. 6 Myr after the end of the salt deposition, there is negligible salt deformation

in the two smaller sub-basins, LSb1-2, part of the proximal domain (Figure 4b). In the centre of LSb3, within the proximal domain, a >1.5 km tall upright diapir forms where the salt is the thickest, together with a small salt anticline further seaward (Figure 4b). The diapir reaches the seafloor and is bounded on both sides by broadly symmetric minibasins with localized, near-diapir stratal upturn. In the distal sub-basin (Sb4), there is a more widespread and variable salt deformation. There is seaward salt expulsion and development of a ca. 1 km thick seaward-dipping rollover at the transitional domain, underneath the shelf-break, and salt inflation with the development of broad (ca. 2–3 km wide and 1–2 km tall) diapirs and small anticlines above the distal FB and distal margin domain (Figure 4b). A ca. 22 km wide salt nappe with subtle salt anticlines and diapirs forms at the downdip end of LSb4, advancing over exhumed lower crust and newly-formed oceanic crust (Figure 4b). This nappe is initiated by ca. 15 km of salt stretching as the two conjugate salt basins separate and is later amplified by ca. 9 km of post-rift nappe advance, forming a ca. 24 km wide salt nappe (cf. Pichel et al., 2022a, 2022b).

By 23 Myr, most of the salt structures have been amplified. The proximal, upright diapir continues rising, reaching a height of ca. 3.5 km while its surrounding minibasins thicken and subside (Figure 4c). In Sb4, there is increasing seaward salt expulsion and rollover amplification with the development of a landward-dipping normal fault and a hybrid, expulsion-extension rollover at the transitional domain, underneath the shelf-break (Figure 4c). Further seaward, over the distal FB and salt nappe, the earlier diapirs and anticlines evolve into narrow (ca. 1–2 km wide) and tall (ca. 4–5 km) diapirs with various shapes separated by intervening minibasins (Figure 4c). The most proximal diapirs have upright to seaward-leaning geometries with squeezed feeders and are associated with slightly rotated minibasins, whereas the ones located over the salt nappe are broader and with simpler, symmetrical minibasins (Figure 4c). Between 18 and 23 Myr, the salt nappe advances ca. 6 km further seaward, reaching a total width of ca. 30 km (Figure 4c).

The proximal, upright diapir continues to rise and the seaward-dipping hybrid rollover amplifies, and its underlying normal fault accommodates a total of ca. 5 km of extension by 30 Myr (Figure 4c,d). There is also continued rise and squeezing of most diapirs further seaward in Sb4, but negligible additional translation of the salt nappe and its overlying salt structures apart from its most distal seaward-leaning diapir, indicating updip extension is balanced downdip by diapir squeezing (Figure 4d). At the end of the model, 40 Myr, there is only limited additional rise and a slight narrowing of the most proximal diapir (Figure 4e). The seaward-dipping rollover grows further, reaching a total thickness of ~6 km, while its underlying fault accommodates a total of ca. 10 km of extension (Figure 4). This extension is accommodated further downdip by diapir squeezing above the distal salt nappe with most diapirs rising an additional ca. 1–2 km. The intervening minibasins thicken and reach up to 5–6 km of thickness (Figure 4e). No additional salt nappe advance occurs between 30 and 40 Myr.

3.2 | High constant sediment flux model M2

For the same margin architecture and width, the high constant sediment flux model M2 exhibits a notably different distribution and magnitude of deformation, although the overall style remains similar to the reference case (cf., Figure 5a,b; see Video S2 for evolution). There is no salt deformation in the most proximal sub-basins LSb1-3 in M2 (Figure 5a), whereas in reference model M1, a prominent ca. 6 km tall diapir forms in LSb3 (Figure 5a). Over LSb4, in the transitional margin domain, there is the development of a ca. 5 km thick seaward-dipping hybrid rollover associated with a pair of vertically offset 1–1.5 km tall landward-dipping listric faults and a broad (ca. 3 km tall) diapir (Figure 5a). These normal faults accommodate a total of ca. 5 km of overburden extension in the transitional margin domain (Figure 5a). In the reference model (M1), the equivalent seaward-dipping rollover is located ca. 12 km further landward, at the updip edge of LSb4, and is bounded by a single larger fault that accommodates a total of ca. 10 km of overburden extension with only minor salt rise (<1 km) in its footwall (Figure 5b). Significant differences also occur between the high sediment flux model and the reference model in the distal domain where a narrower, ca. 24 km wide salt nappe forms over the exhumed lower continental crust and oceanic crust (Figure 5a), as opposed to a ca. 30 km wide nappe in the reference model (Figure 5b). There is also less diapirism and diapir squeezing, in the high sediment flux model with the development of only two, upright and moderately squeezed diapirs, in contrast to seven, highly squeezed and mostly seaward-leaning diapirs in the reference model (Figure 5a,b). M2 also develops a small (ca. 1.5 km tall) thrust-fed seaward-leaning diapir at the distal edge of the salt nappe.

3.3 | Low constant sediment flux model M3

In the low sediment flux model M3, there is a general increase in the complexity and number of salt structures

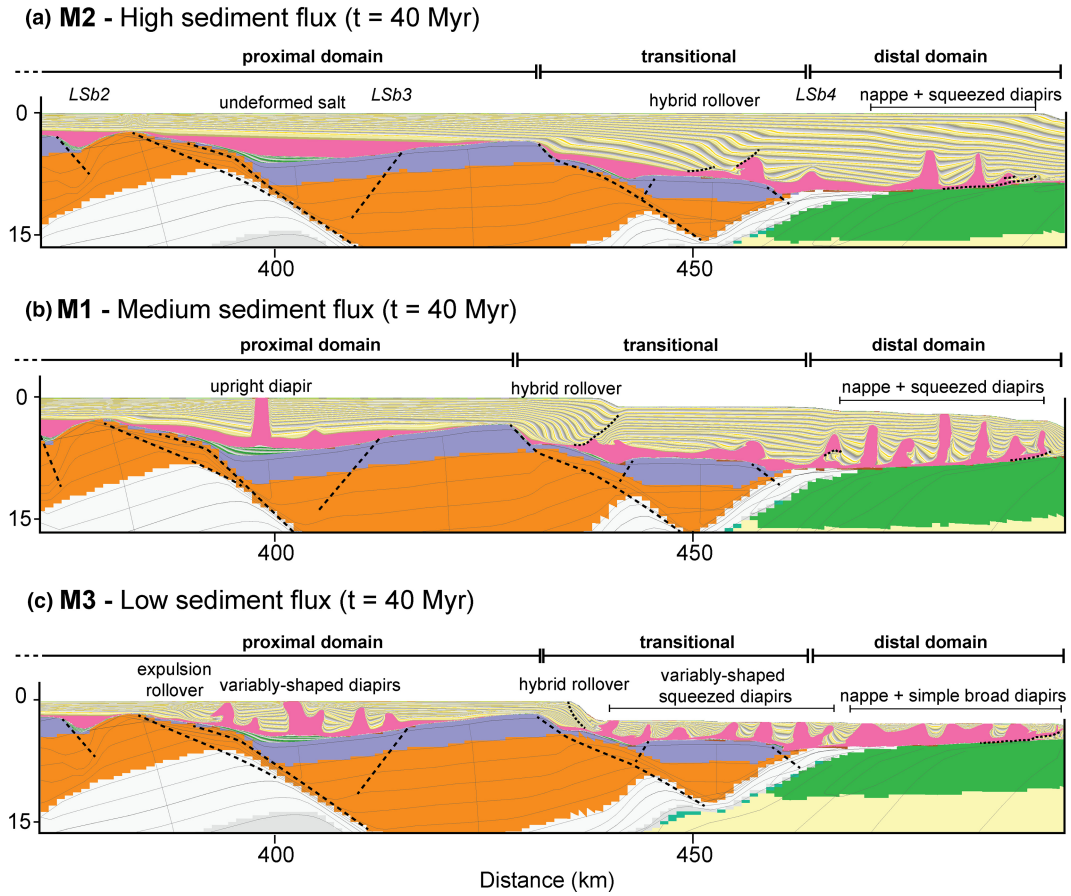

FIGURE 5 Models of intermediate-width margin with different, but constant, post-rift sediment fluxes at their final stages, 40 Myr. (a) M2—high-flux (30 km^3/Myr), (b) M1—medium flux (15 km^3/Myr) and (c) M3—low flux (7.5 km^3/Myr). Faults in black dashed lines. Different domains of salt deformation are indicated at the top of the models.

(Figure 5c). As in the other models, there is no deformation in the most proximal sub-basins (LSb1-2, Figure 5). There is, however, significantly more pronounced salt deformation in LSb3, with the development of five complex diapirs compared to only one to no diapir in the higher sediment flux models M1 and M2 (Figure 5). These diapirs vary from ca. 3 to 5 km tall, squeezed geometries with salt tongues to simple triangular and broadly symmetric shapes with either bowl- or wedge-shaped fill/internal geometries (Figure 5c). The most proximal of these diapirs is bounded landward by a prominent expulsion rollover, which does not form in the previous models (Figure 5). Another striking difference is that some of the proximal minibasins display abrupt shifting of depocentres seaward towards the adjacent diapirs (Figure 5c).

The proximal edge of LSb4 is characterized by a seaward-dipping rollover above depleted salt that is cross-cut by a steep seaward-dipping normal fault located directly beneath the shelf-break and above the top of a seaward-dipping base-salt ramp (Figure 5c). This rollover transitions laterally into a ca. 3 km tall seaward-leaning squeezed diapir at the base of the same base-salt ramp (Figure 5c). In contrast to the models with higher sediment flux, there is significant diapirism over the distal FB in the proximal part of LSb4 with the development of four squeezed diapirs with variable size and shape, and complex intervening minibasin geometries (Figure 5c). These include expulsion rollovers, bowl- and wedge-shaped minibasin fill with shifting depocentres. In the distal domain, the salt nappe reaches ca. 32 km in width, the widest of all three constant sediment flux models (Figure 5). The nappe is associated with the same number of diapirs as the reference model, but the diapirs are in general broader (ca. 2–3 km tall and 3–4.5 km wide) and with simpler, bowl-shaped minibasins (Figure 5).

3.4 | Low sediment flux with early post-rift pulse model M4

Model M4 with an early post-rift sediment pulse and low background sediment flux shows overall similar proximal and distal deformation styles to what is observed in the low flux model M3, but key differences occur in the transitional domain which was the locus of deposition during

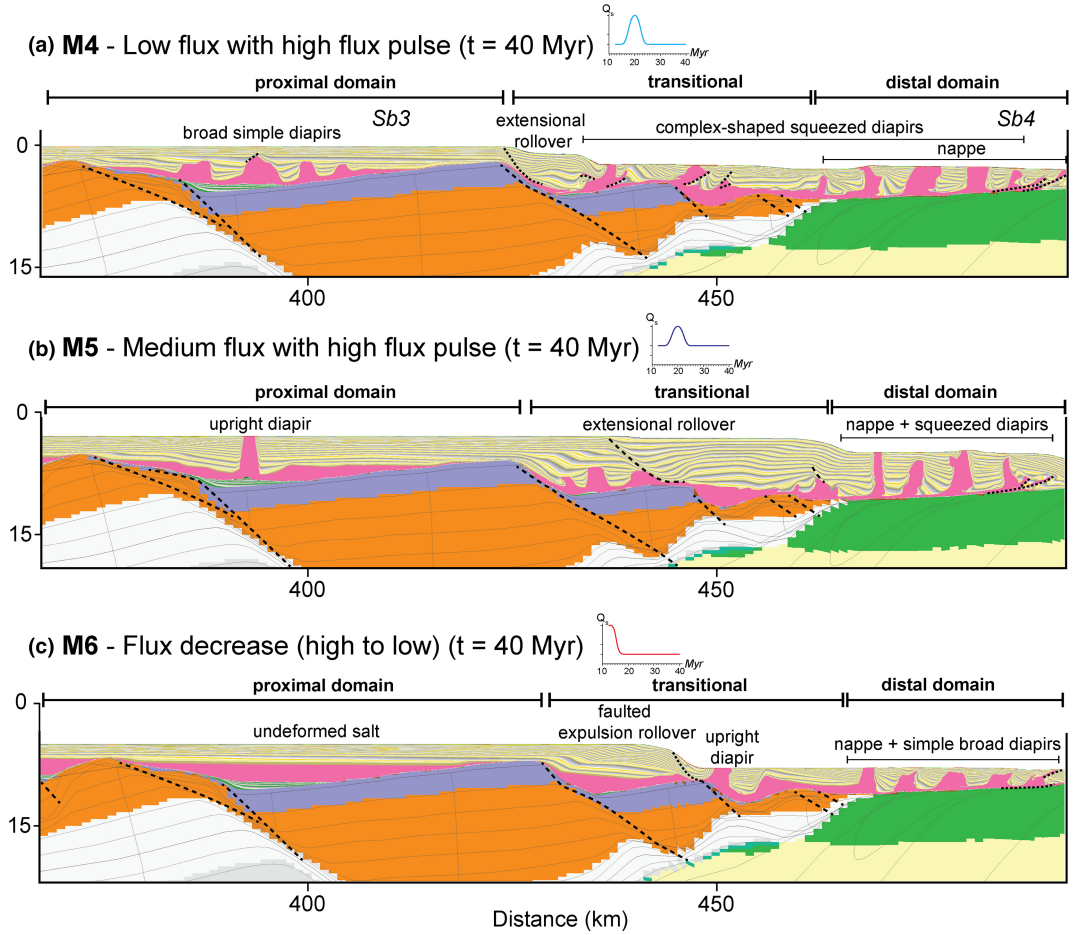

FIGURE 6 Models of intermediate-width margin with different, time-varying post-rift sediment fluxes at their final stages, 40 Myr. (a) M4—low-high-low flux, (b) M5—medium-high-medium-flux and (c) M6—high-low flux. Faults in black dashed lines. Different domains of salt deformation are indicated at the top of the models. Curves of sediment flux variation over time are presented for each model.

the sediment flux pulse (Figure 6a). In the proximal domain, there is a similar frequency of diapirs to the low flux model M3, although in M4, they are generally broader, more upright and with simpler bowl- and wedge-shaped minibasins (cf. Figures 5c and 6a). The transitional domain is notably different from any of the constant-flux models. It exhibits minibasins and a large extensional rollover bounded by a basinward-dipping normal fault passing seaward into complex-shaped diapirs associated with salt tongues, thrusts and significant near-diapir stratal upturn. The distal domain contains a set of ca. 3–4 km tall, broadly upright squeezed diapirs overlying the distal salt nappe, similar to the medium flux model M1, albeit with different dimensions. The most proximal diapirs are narrower and more complex, being associated with significant tilting and shifting of minibasins depocentres, whereas the most distal diapirs are broader and simpler with more upright and predominantly bowl-shaped minibasin fill. Small, seaward-leaning diapirs form by thrusting at the distal end of the salt nappe, which reaches a total width of ca. 30 km (Figure 6a). The frequency, size, complexity and geometry of the diapirs and their associated minibasins in the distal domain are similar to the medium flux model M1, but the width of the underlying salt nappe is similar to the low flux model M3 (Figure 5c).

3.5 | Medium sediment flux with early post-rift pulse model M5

In the case of a medium background sediment flux with an early post-rift sediment pulse, the proximal and distal deformation domains are similar to the medium constant flux model M1 (cf. Figures 5a and 6b). As with M4, there are large differences in the transitional domain. There, two small (<3 km), upright diapirs pass seaward into a ca. 1 km tall salt triangular diapir in the footwall of a basinward-dipping listric normal fault which has a ca. 6 km thick landward-dipping extensional rollover in its hanging wall. This normal fault and rollover are larger and occur ca. 10 km further basinward than in M4, being located over the crest of the distal fault-block, and it has

a different polarity to that in the medium flux model M1 (cf. Figure 6a,b). The distal domain is similar to medium flux model M1 with four ca. 4–5 km tall, broadly upright squeezed diapirs overlying the distal salt nappe (Figures 5b and 6b), and to model M4, although, in M5, the diapirs are narrower and slightly taller. The nappe is also slightly narrower, reaching a total width of ca. 26 km (Figure 6b).

3.6 | Early post-rift sediment flux decrease model M6 (high to low flux)

In the case of an initially high sediment flux that decreases to a low flux over 5 Myr, there is no salt deformation in the proximal domain, identically to high flux model M2 (Figures 5a and 6c). The transitional domain is overall similar to the medium flux model M1. It contains a large seaward-dipping expulsion rollover offset by a basinward-dipping normal fault passing seaward into a ca. 4 km tall upright diapir with a bowl-shaped minibasin and a broad (ca. 5 km wide) salt anticline. Further seaward, the style of deformation is similar to low flux model M3 (Figure 5c) with five, generally broad and simple diapirs with slightly rotated minibasins over a ca. 26 km wide distal salt nappe (Figure 6c).

3.7 | Sensitivity to post-salt sediment density

Models testing different post-salt sediment densities show that when the post-salt sediment density is equal to the salt density (SM7), there is negligible diapirism across the entire margin and overall simpler salt tectonics compared to the reference model M1 (Figure S1). In SM7 (Figure S1a), only the transitional domain develops an extension-driven diapir associated with a hybrid rollover, similar to the reference model. In contrast, the proximal domain remains completely undeformed and the distal domain is associated mostly with lateral salt tectonics including salt nappe advance, inflation and anticlines, but it develops no diapirs (cf., Figure 1a,c). In SM8 (Figure S1c), where the post-salt sediment density is higher than the salt but less than in M1, there is still diapirism in the transitional and distal domains, but their magnitude and complexity are less (cf. Figure 1b,c). The proximal domain forms no diapirs but deforms mildly, as opposed to SM7, by forming subtle salt anticlines (Figure 1c), exhibiting in general an intermediate scenario between M1 and SM7.

3.8 | Structural processes quantifications

In this section, we describe and quantify the main salt-related features and structural processes and how these vary according to the different post-salt sediment fluxes (Figure 7). For simplification, we focus our quantitative analysis on the constant flux model set.

Gravity-driven updip overburden extension and downdip diapir shortening are the greatest for the medium post-salt sediment fluxes and the lowest for the high flux (Figure 7a). Both processes are related to the lateral translation of both salt and overburden (cf., Peel, 2014; Rowan et al., 2004), and thus are driven by Couette salt flow. Pressure-driven Poiseuille flow, in which only the salt translates laterally, is estimated by the balancing of margin-scale salt deformation (cf., Pichel et al., 2022b) and its contribution decreases with increasing post-salt sediment flux (Figure 7a). Nappe width is a product of late syn-rift salt stretching and post-rift salt advance, which is mostly related to pressure-driven Poiseuille flow. Syn-rift salt stretching is equal for all models as their rift evolution, margin architecture and timing and thickness of salt deposition do not vary, whereas post-rift salt advance and, therefore, nappe width increase with decreasing post-rift sediment flux (Figure 7b). The lateral rate of salt flow (V_s) is estimated by the sum of Couette and Poiseuille flow contributions for seaward salt motion. This rate, V_s, is the largest for the medium sediment flux and lowest for the high flux, which in turn also produces the lowest ratio between lateral (Couette-flow) and vertical (diapirism) salt tectonics for the medium post-salt flux (Figure 7c). The estimated Couette flow rate (V_c) is also greatest for the medium sediment flux, whereas the Poiseuille flow rate (V_p) decreases with increasing post-salt sediment flux (Figure 7d).

4 | DISCUSSION

4.1 | The influence of post-salt sedimentation on the magnitudes and styles of salt tectonics

All models have equal margin and salt basin architecture, base-salt relief and initial salt distribution and thickness allowing us to isolate the effects of variable sedimentation on regional and local salt flow. We compare these models and their respective domains (proximal, transitional and distal) in terms of magnitude and styles of (i) seaward salt flow, (ii) diapirism, (iii) overburden extension and (iv) distal nappe advance as a function of the relationship between post-salt sediment progradation rate (V_{prog}) and salt flow rate (V_s). In general, when the post-salt progradation rate (V_{prog}) is considerably higher than the rate of salt flow

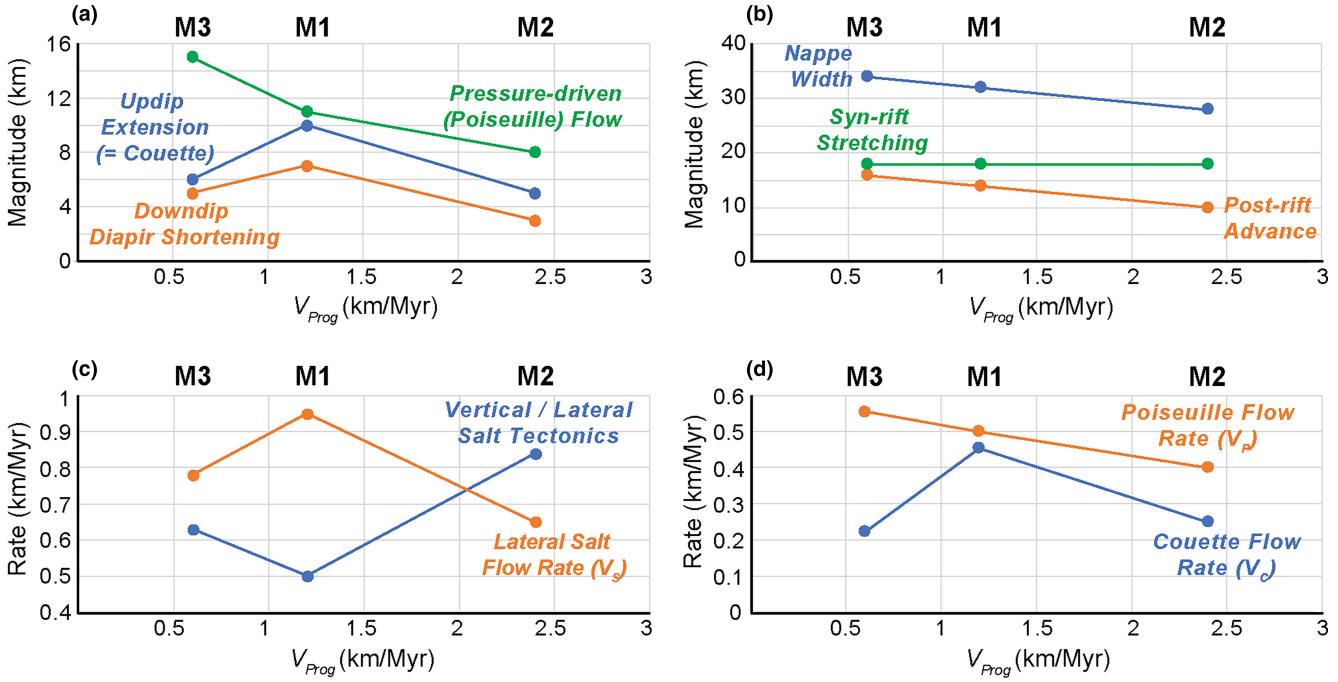

FIGURE 7 Structural processes quantification plots as a function of variable progradation rates (V_{prog}) for the three constant flux models (M1–M3): (a) magnitudes of updip extension, downdip diapir shortening and pressure-driven (Poiseuille) salt flow. (b) Salt nappe processes including the final nappe width, a product of syn-rift stretching and post-rift nappe advance. (c) Lateral salt flow rate (V_s,) and the ratio between vertical (diapirism) and lateral salt tectonics. (d) Poiseuille (V_p) and Couette (V_c) flow rates.

(V_s), the salt is buried by the rapidly prograding sediments and salt flow, either vertical (i.e. diapirism) or lateral, is suppressed (Figures 5a and 8a). Conversely, if the post-salt progradation rate (V_{prog}) is lower or equal to the rate of lateral salt flow (V_s), the salt is evacuated seaward over a seaward-dipping base-salt and, secondarily by vertical flow into growing diapirs (Figure 8).

4.1.1 | Proximal domain

In the proximal domain, where there is negligible lateral salt flow owing to the isolation of the proximal sub-basin by a base-salt high, the salt volume remains constant through time. There, we observe an inverse relationship between V_{prog} and diapirism (Figure 8). In the high-flux model M2, $V_{prog} > V_s$, there is no salt deformation in the proximal domain (Figure 8a). In medium flux model M1, $V_{prog} \sim V_s$ allows the development of a single, upright diapir in the centre of the sub-basin where the salt was originally thicker (Figure 8b). In low flux model M3, where $V_{prog} < V_s$, a series of variably shaped and complex diapirs and minibasins with shift of depocentres develop owing to the switch of salt flow between adjacent diapirs (Figure 9c). The medium flux model M1, however, develops the largest of these diapirs owing to the greater volume of sediments deposited in the intervening minibasins and the lack of competition for salt supply between adjacent diapirs (Figure 5b).

4.1.2 | Transitional and distal domains

In the transitional and distal domains, the salt is connected and able to flow laterally from the former to the latter which produces a more complex relationship between the rate of progradation (V_{prog}), sediment volume and salt flow (V_s).

High-flux sedimentation suppresses most salt tectonic deformation in the transitional domain allowing for minor diapirism, formation of a hybrid rollover and a landward-dipping normal fault that accommodates minor, ca. 5 km, of overburden extension (Figure 8a). Post-salt sediments also quickly cover the distal margin, allowing only minor diapirism and nappe advance in this domain (Figure 8a). The magnitude of deformation in these domains is greater than in the proximal domain owing to (i) the lack of a significant distal base-salt high that buttress seaward salt flow, (ii) salt being able to start flowing relatively earlier to the arrival of a significant volume of sediments during margin progradation and (iii) the seaward dip of the salt basin in the transitional domain which favours seaward salt flow onto the distal domain and the salt nappe. The overall magnitude

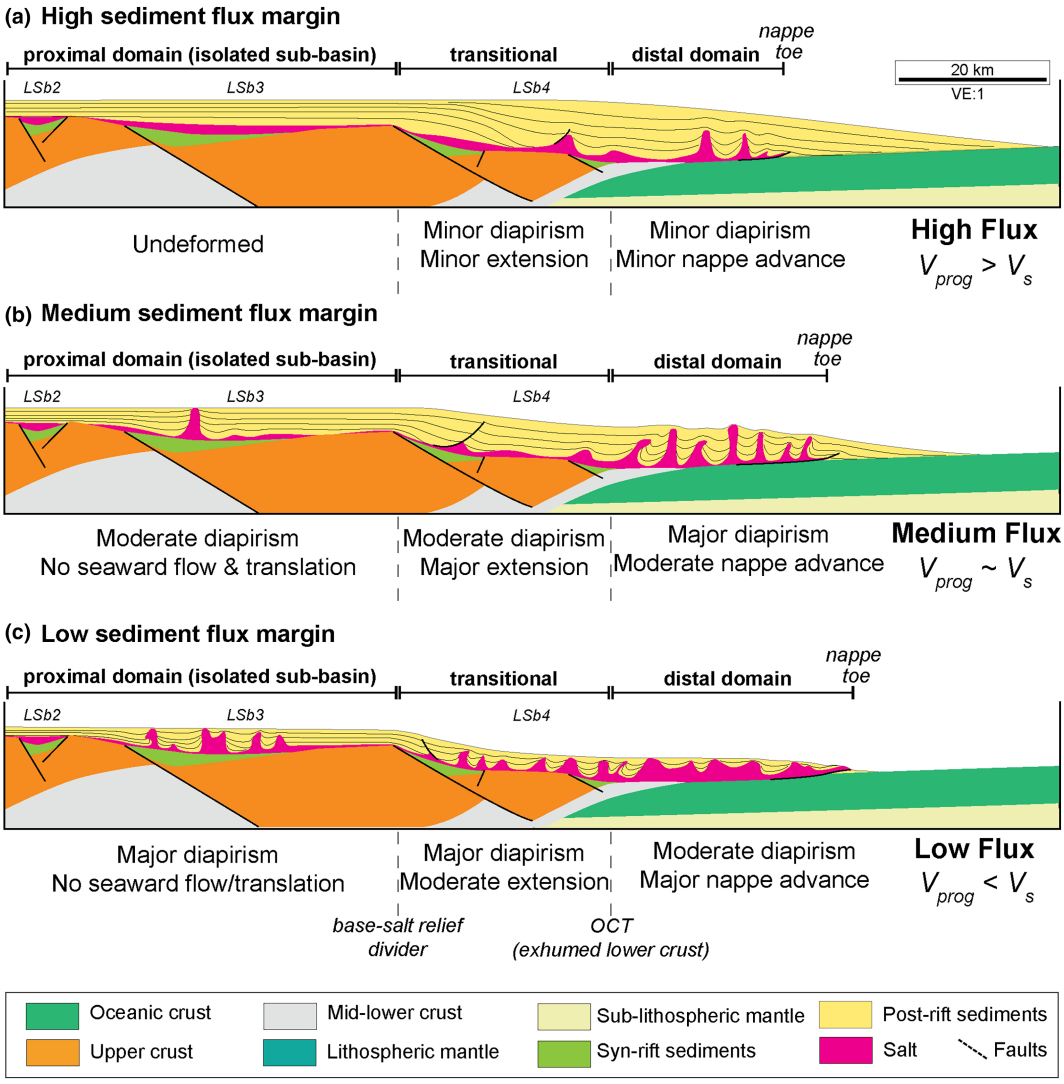

FIGURE 8 Summary diagram illustrating the contrasts in the styles and magnitude of salt tectonic processes (diapirism, seaward salt flow, updip extension and nappe advance) across different structural domains (proximal, transitional and distal) for different post-salt sediment fluxes and progradation rates: (a) high flux, (b) medium flux and (c) low flux. The differences are primarily controlled by the relationship between the rates of sediment progradation rate (V_{prog}) and salt flow (V_s).

of salt deformation, that is, seaward salt flow, diapirism, overburden extension and shortening and nappe advance, is nonetheless low compared to the other models (Figure 8).

On the other end of the spectrum, low post-salt sediment flux promotes significant salt flow resulting in major diapirism and moderate overburden extension (ca. 6 km) in the transitional domain, and major nappe advance (ca. 16 km) and moderate diapirism in the distal domain (Figure 8c). Medium sediment flux reduces diapirism in the transitional domain but produces greater overburden extension (ca. 10 km) compared to the low sediment flux case. Later arrival of post-salt sediments in the distal domain compared to the high flux case allows for more pronounced diapirism with the formation of multiple and more complex diapirs and moderate nappe advance (ca. 14 km; Figure 8b). This demonstrates that seaward salt flow onto the distal nappe is greater for lower sediment fluxes in which $V_{prog} < V_s$, but the magnitude of overburden updip extension, translation and downdip diapir shortening are greater for medium fluxes, where $V_{prog} \sim V_s$.

This greater overburden extension and translation are directly related to the Couette salt flow component (V_c; Figure 7). The measured V_c is larger for the medium flux model M1 because the salt in the transitional domain is neither rapidly buried as in the high flux model M2 (Figure 9a), nor rapidly evacuated seaward as in the low flux model M3 (Figure 8c). Thus, there are both enough salt and overburden to extend and record lateral salt flow in this domain for the medium flux model M1 (Figure 4). The earlier and greater seaward salt flow onto the distal salt nappe in the low-flux model is a product of both

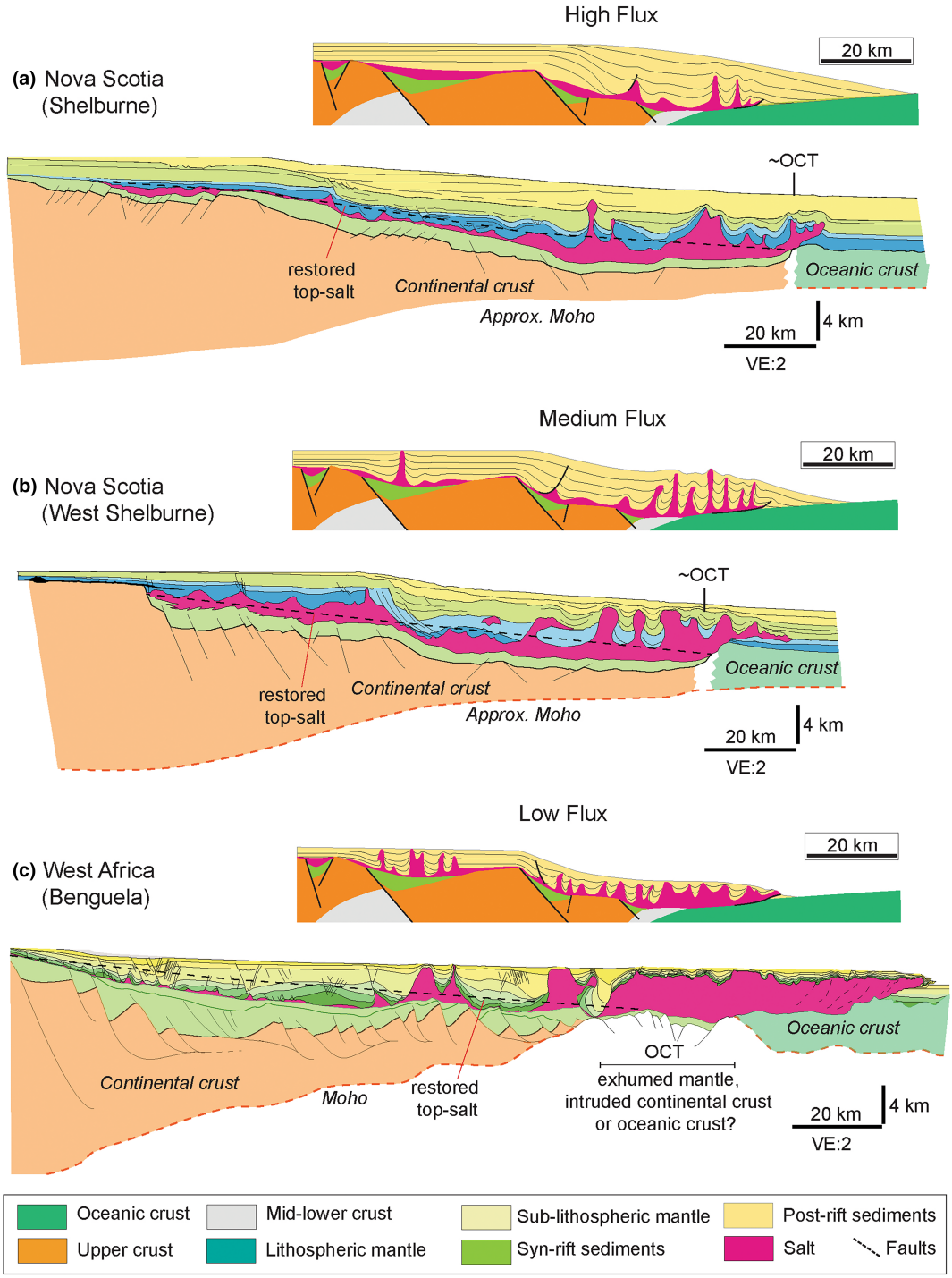

FIGURE 9 Comparison of model results with natural rifted margin salt tectonics: (a) Shelburne Basin, and (b) West Shelburne Basin, Nova Scotia adapted and depth-converted from Deptuck and Kendell (2017). The approximated Moho (dashed orange line) and the depth conversion were based on refraction data from Wu et al. (2006). (c) Benguela Basin, West Africa, adapted from Pichel et al. (2023).

Poiseuille (V_{prog}) and Couette flow (V_c). The magnitude (P) and rate of pressure-driven flow (V_p) are the greatest in the low-flux model owing to the lowest volume of sediments being deposited in the distal margin throughout the model evolution, which in turn creates a greater differential sediment loading between transitional and distal domains. We note that the salt flow profile varies through time and space across the margin. Although post-rift nappe advance is controlled by pressure-driven salt flow (P), with salt expulsion from the transitional domain into the nappe, the local flow profile within the nappe is primarily Couette (C), owing to the lack of sediments directly overlying the nappe (see animations in Supplementary material). This lack of distal overburden sediments results in this early

Couette flow not being recorded by overburden extension or shortening.

The magnitude and complexity of diapirism increase with decreasing post-salt sediment flux and V_{prog} in the transitional domain as in the proximal domain, but not in the distal domain, where diapirism complexity and magnitude are greater for the medium flux model M1 (Figure 8). This is explained by: (i) a greater volume of sediments deposited within minibasins in the distal domain, and (ii) the greater downdip diapir shortening in response to the updip extension for the medium flux model, both of which contribute to greater vertical salt flow into rising diapirs.

4.1.3 | Effect of time-varying sediment flux

In cases where sediment flux changes through time, its effect on post-salt differential sediment loading, and structural variability are more localized, occurring mainly in the transitional domain, which is the main locus of deposition during the change in sediment flux (Figure 6). The distal domain is also affected owing to the variable amount of salt expelled from the transitional domain, but the proximal domain is nearly identical to their equivalent constant flux model (Figures 5 and 6). The transitional domain has greater complexity and variability of salt structures, including diapirs and rollovers with different geometries and/or fault polarities, in models with time-varying fluxes relative to constant fluxes (Figures 5 and 6). This contrast is even more conspicuous in models with an increase followed by a decrease in sediment flux, which forms prominent and complex diapirs, many of which have salt tongues and overturned minibasins that transition onto expulsion rollovers (Figure 6a) or large extensional rollovers (Figure 6b). For the case of a simpler gradual decrease of sediment flux (from high to low flux), the proximal domain is similar to the high flux model M2 and the distal domain to the low flux model M3. The transitional domain displays a more in-between scenario, with salt and minibasin geometries more comparable to the low flux model M3 but with the number of structures being the same as the high flux model M1.

4.2 | Comparison with natural examples

The rifted margin architecture and the salt tectonic geometries and evolution from our numerical models are comparable to various salt-bearing rifted margins across the globe, in particular, the ones with late syn-rift salt in the Gulf of Mexico and parts of the South-Central Atlantic Ocean. Our comparison is however restricted to the limited public availability of regional high-quality seismic profiles. In most cases, the ones available show good quality and resolution for either post-salt structures or pre-salt rift architecture, but rarely both. In many instances, these profiles are in two-way-time so they require depth conversion to ensure accurate quantification of salt and post-sediment thickness and comparison with our models. Moreover, seismic profiles only show the final, present-day stage of deformation. These limitations however highlight the value of our numerical models in helping to solve the often-obscure link between margin-scale rift architecture and salt tectonics, and to aid in the interpretation of typically poorly imaged pre-salt structures and/or highly deformed salt and post-salt intervals.

We compare our models to published examples from the Nova Scotia margin (Deptuck & Kendell, 2017) and West Africa (Pichel et al., 2023), more specifically the Shelburne and West Shelburne segments in Nova Scotia and the Benguela from West Africa. These examples present different crustal structures but an overall similar margin and salt basin width to our intermediate-width margin models, varying ca. 130–160 km (±10 km; Figure 9). Due to the lack of data coverage and/or uncertainties in the sub-salt, and because our models focus on analysing the link between post-salt sediment flux and thickness on salt tectonics, we do not compare nor discuss sub-salt features between these profiles and our models.

The Shelburne segment of Nova Scotia displays a ca. 140–145 km wide margin with a restored salt basin width of ca. 140 km (Figure 9a). The average post-salt sediment thickness is ~6.2 km in the mid-lower slope. Salt thickness varies from ca. 1 to 1.5 km in the proximal and transitional domains to ca. 2.5–3 km in the deep-basin in the distal domain. The profile shows negligible salt deformation in the proximal domain with only subtle salt folding in the proximal, largely isolated salt sub-basin (Figure 9a). The transitional domain shows also relatively limited salt deformation, mostly associated with seaward salt evacuation and the development of small (<1 km tall) extensional diapirs and normal faults. The distal domain displays more pronounced salt tectonics with the development of a set of three large, 3–4 km tall, upright and simple diapirs associated with bowl-shaped minibasins and a few smaller diapirs over a ~10 km wide salt nappe. The salt basin width and thickness, the average post-salt sediment thickness and the overall style and magnitude of salt deformation are strikingly similar to our high flux model M2 (Figure 9a).

The West Shelburne segment comprises a ca. 130 km wide margin with an equally wide salt basin (Figure 9b). The restored salt thickness varies from ca. 1 km in the proximal domain to ca. 2–2.5 km in the distal domain, being slightly less variable than in the previous example (Figure 9a,b). Post-salt sediment thickness is on average

ca. 4.7 km in the mid-lower slope. The profile shows a more pronounced style of salt deformation across the entire margin segment (Figure 9b). There are a few ca. 1–2 km diapirs and/or salt anticlines in the proximal domain, and a pronounced ca. 10 km wide rollover in the transitional domain where the base-salt steepens. The distal domain exhibits a ca. 16 km wide salt nappe and a series of ca. 4–5 km tall, highly squeezed diapirs associated with bowl- and wedge-shaped minibasins and occasionally salt tongues and tear-drop geometries (Figure 9b). The initial geometry and thickness of the salt basin as well as the average post-salt sediment thickness and the style, magnitude and complexity of salt tectonics are similar to our reference, medium flux model M1 (Figure 9b). A few differences do however occur such as the polarity of the large rollover and its associated normal fault in the transitional domain and the style of diapirism in the proximal domain. We interpret the latter to be associated with a greater salt thickness and connectivity between the proximal and distal salt. The former is interpreted to be caused by the likely temporal variability of post-salt sediment flux in the transitional domain, which generates similar structures and style and magnitude of extension in all our time-varying flux models (M4–M6).

The Benguela margin is ca. 130–160 km wide, this range depends on the interpretation of exhumed mantle, intruded continental crust or early oceanic crust at the ocean–continent transition (Figure 9c). The restored salt basin displays a similar width, ca. 140 km (see Pichel et al., 2023). The salt is more broadly distributed and connected than in the previous examples with an average salt thickness of ca. 1.5–2 km, being generally thicker in the centre of the salt basin and pinching out towards both its proximal and distal edges (Figure 9c). The post-salt sediment thickness is on average ca. 4 km in the mid-slope, comparable to our low flux model M3 with ca. 3–3.5 km of post-salt sediment thickness in the mid-lower slope. The proximal domain in this profile does not compare as well as the previous ones to our models due to the greater proximal salt connectivity and regional seaward-dipping base-salt in Benguela. This produces limited vertical diapir growth but significant seaward salt evacuation and overburden extension with the development of a series or <1 km tall salt rollers and normal faults in the proximal domain, as opposed to tall, upright diapirs and bowl-shaped minibasins over a broadly flat salt sub-basin in our model (Figure 9c). The transitional domain, however, presents more similarities with the occurrence of a large basinward-dipping normal fault and a salt roller and further seaward with simple, sinusoidal-shaped diapirs wedge-shaped minibasins and/or turtle anticlines (Figure 9c). A large, complex-shaped diapir with a seaward-verging tear-drop structure overlying a highly rotated minibasin forms in the transition to the distal domain, at the transition to exhumed or newly formed crust as in our low flux model M3. The distal domain is characterized by a ca. 35 km wide, inflated (ca. 3.5–4 km thick) salt nappe with simple, generally broad salt diapirs and anticlines, also similar to our low flux model M3 (Figure 9c).

5 | CONCLUSIONS

Our geodynamic numerical models illustrate how variable post-salt sediment fluxes and progradation rates promote significant differences in the styles and magnitude of salt tectonics across salt-bearing rifted margins. All models presented here have a broadly identical rifted margin and salt basin architecture that allow us to isolate the effects of post-salt sedimentation on margin-scale salt tectonics from proximal to distal domains for intermediate-width margin types. There are major differences in the degree of seaward salt flow, diapirism, overburden extension, downdip shortening and nappe advance which produce contrasting salt and overburden geometries for the same margin type. The differences are primarily controlled by the relationship between the rates of sediment progradation (V_{prog}) and salt flow (V_s). When $V_{prog} \gg V_s$, the salt is rapidly buried and both vertical and lateral salt flow are suppressed across the entire margin. When $V_{prog} < V_s$, the salt flows vertically and seaward over a dipping base-salt faster than sediments prograde producing major diapirism in the proximal domain and major nappe advance in the distal domain, although with only moderate overburden extension and distal diapirism. When $V_{prog} \sim V_s$, there is moderate proximal diapirism and distal nappe advance, but greater overburden updip extension and downdip shortening, which in turn produces major diapirism in the distal domain. The models have clear limitations, such as the use of homogenous salt and overburden, the lack of compaction and their 2D nature, but these are valid approximations to understand the first-order impacts of varying sedimentation patterns on margin-scale salt flow. Future work should thus expand on this and incorporate some of these aspects. Nonetheless, the modelling results are comparable to natural systems and increase our knowledge of the controls and dynamics of salt tectonics along rifted margins worldwide.

ACKNOWLEDGEMENTS

We thank the Equinor-UiB Akademia agreement for funding the project. We also thank Steven Ings and Tim Dooley for the constructive comments during the review and Kerry Gallagher for the excellent editorial handling.

CONFLICT OF INTEREST STATEMENT

The authors declare that they have no conflict of interest.

PEER REVIEW

The peer review history for this article is available at https://www.webofscience.com/api/gateway/wos/peer-review/10.1111/bre.12802.

DATA AVAILABILITY STATEMENT

Data are computed with the equations presented here and in Pichel et al. (2022a, 2022b). All model outputs, graphics and time steps are presented as animations in the supplementary material.

ORCID

Leonardo M. Pichel https://orcid.org/0000-0001-8692-3831
Ritske S. Huismans https://orcid.org/0000-0003-0548-6591
Robert Gawthorpe https://orcid.org/0000-0002-4352-6366
Jan Inge Faleide https://orcid.org/0000-0001-8032-2015

REFERENCES

Albertz, M., Beaumont, C., Shimeld, J. W., Ings, S. J., & Gradmann, S. (2010). An investigation of salt tectonic structural styles in the Scotian Basin, offshore Atlantic Canada: 1. Comparison of observations with geometrically simple numerical models. *Tectonics*, *29*(4), TC4017.

Allen, J., & Beaumont, C. (2016). Continental margin syn-rift salt tectonics at intermediate width margins. *Basin Research*, *28*(5), 598–633.

Allen, J., Beaumont, C., & Deptuck, M. E. (2020). Feedback between synrift lithospheric extension, sedimentation and salt tectonics on wide, weak continental margins. *Petroleum Geoscience*, *26*(1), 16–35.

Baby, G., Guillocheau, F., Braun, J., Robin, C., & Dall'Asta, M. (2020). Solid sedimentation rates history of the southern African continental margins: Implications for the uplift history of the South African Plateau. *Terra Nova*, *32*(1), 53–65.

Davison, I., Anderson, L., & Nuttall, P. (2012). Salt deposition, loading and gravity drainage in the Campos and Santos salt basins. *Geological Society of London Special Publications*, *363*(1), 159–174.

Deptuck, M. E., & Kendell, K. L. (2017). A review of Mesozoic-Cenozoic salt tectonics along the Scotian margin, eastern Canada. In J. I. Soto, J. Flinch, & G. Tari (Eds.), *Permo-Triassic salt provinces of Europe, North Africa and the Atlantic margins* (pp. 287–312). Elsevier.

do Amarante, F. B., Jackson, C. A. L., Pichel, L. M., Scherer, C. M. D. S., & Kuchle, J. (2021). Pre-salt rift morphology controls salt tectonics in the Campos Basin, offshore SE Brazil. *Basin Research*, *33*(5), 2837–2861.

Epin, M. E., Manatschal, G., Sapin, F., & Rowan, M. G. (2021). The tectono-magmatic and subsidence evolution during lithospheric breakup in a salt-rich rifted margin: Insights from a 3D seismic survey from southern Gabon. *Marine and Petroleum Geology*, *128*, 105005.

Erdős, Z., Huismans, R. S., van der Beek, P., & Thieulot, C. (2014). Extensional inheritance and surface processes as controlling factors of mountain belt structure. *Journal of Geophysical Research: Solid Earth*, *119*(12), 9042–9061.

Gemmer, L., Ings, S. J., Medvedev, S., & Beaumont, C. (2004). Salt tectonics driven by differential sediment loading: Stability analysis and finite-element experiments. *Basin Research*, *16*(2), 199–218.

Gleason, G. C., & Tullis, J. (1995). A flow law for dislocation creep of quartz aggregates determined with the molten salt cell. *Tectonophysics*, *247*(1–4), 1–23.

Goteti, R., Beaumont, C., & Ings, S. J. (2013). Factors controlling early stage salt tectonics at rifted continental margins and their thermal consequences. *Journal of Geophysical Research: Solid Earth*, *118*(6), 3190–3220.

Hudec, M. R., & Jackson, M. P. (2004). Regional restoration across the Kwanza Basin, Angola: Salt tectonics triggered by repeated uplift of a metastable passive margin. *AAPG Bulletin*, *88*(7), 971–990.

Hudec, M. R., & Jackson, M. P. (2007). Terra infirma: Understanding salt tectonics. *Earth-Science Reviews*, *82*(1–2), 1–28.

Hudec, M. R., & Norton, I. O. (2019). Upper Jurassic structure and evolution of the Yucatán and Campeche subbasins, southern Gulf of Mexico. *AAPG Bulletin*, *103*(5), 1133–1151.

Hudec, M. R., Norton, I. O., Jackson, M. P., & Peel, F. J. (2013). Jurassic evolution of the Gulf of Mexico salt basin. *AAPG Bulletin*, *97*(10), 1683–1710.

Jackson, M. P., & Hudec, M. R. (2017). *Salt tectonics: Principles and practice*. Cambridge University Press.

Jackson, M. P., Hudec, M. R., Jennette, D. C., & Kilby, R. E. (2008). Evolution of the cretaceous Astrid thrust belt in the ultradeep-water lower Congo Basin, Gabon. *AAPG Bulletin*, *92*(4), 487–511.

Karato, S. I., & Wu, P. (1993). Rheology of the upper mantle: A synthesis. *Science*, *260*(5109), 771–778.

Kukla, P. A., Strozyk, F., & Mohriak, W. U. (2018). South Atlantic salt basins–Witnesses of complex passive margin evolution. *Gondwana Research*, *53*, 41–57.

Lentini, M. R., Fraser, S. I., Sumner, H. S., & Davies, R. J. (2010). Geodynamics of the central South Atlantic conjugate margins: Implications for hydrocarbon potential. *Petroleum Geoscience*, *16*(3), 217–229.

Marton, L. G., Tari, G. C., & Lehmann, C. T. (2000). Evolution of the Angolan passive margin, West Africa, with emphasis on post-salt structural styles. *Geophysical Monograph-American Geophysical Union*, *115*, 129–150.

Mohriak, W. U., & Leroy, S. (2013). Architecture of rifted continental margins and break-up evolution: Insights from the South Atlantic, North Atlantic and Red Sea–Gulf of Aden conjugate margins. *Geological Society, London, Special Publications*, *369*(1), 497–535.

Peel, F. J. (2014). The engines of gravity-driven movement on passive margins: Quantifying the relative contribution of spreading vs. gravity sliding mechanisms. *Tectonophysics*, *633*, 126–142.

Peel, F. J., Travis, C. J., & Hossack, J. R. (1995). Genetic structural provinces and salt tectonics of the Cenozoic offshore US Gulf of Mexico: A preliminary analysis. In M. P. A. Martin, D. G.

Roberts, & S. Snelson (Eds.), *Salt tectonics: A global perspective*. AAPG Memoir (Vol. *65*, pp. 153–175). American Association of Petroleum Geologists.

Pichel, L. M., Huismans, R. S., Gawthorpe, R., Faleide, J. I., & Theunissen, T. (2022a). Late-syn- to post-rift salt tectonics on wide rifted margins—Insights from geodynamic modelling. *Tectonics*, *41*, e2021TC007158.

Pichel, L. M., Huismans, R. S., Gawthorpe, R., Faleide, J. I., & Theunissen, T. (2022b). Coupling crustal-scale rift architecture with passive margin salt tectonics: A geodynamic modeling approach. *Journal of Geophysical Research: Solid Earth*, *127*(11), e2022JB025177.

Pichel, L. M., Huuse, M., Redfern, J., & Finch, E. (2019). The influence of base-salt relief, rift topography and regional events on salt tectonics offshore Morocco. *Marine and Petroleum Geology*, *103*, 87–113.

Pichel, L. M., Jackson, C. A. L., Peel, F., & Dooley, T. P. (2020). Base-salt relief controls salt-tectonic structural style, São Paulo Plateau, Santos Basin, Brazil. *Basin Research*, *32*(3), 453–484.

Pichel, L. M., Jackson, C. A. L., Peel, F., & Ferrer, O. (2021). The Merluza graben: How a failed spreading center influenced margin structure, and salt deposition and tectonics in the Santos Basin, Brazil. *Tectonics*, *40*(10), e2020TC006640.

Pichel, L. M., Legeay, E., Ringenbach, J.-C., & Callot, J.-P. (2023). The salt-bearing rifted margins in West Africa—Regional structural variability and salt tectonics between Gabon and Namibia. *Basin Research*, in review.

Pichel, L. M., Peel, F., Jackson, C. A.-L., & Huuse, M. (2018). Geometry and kinematics of salt-detached ramp syncline basins. *Journal of Structural Geology*, *115*, 208–230. https://doi.org/10.1016/j.jsg.2018.07.016

Quirk, D. G., Schødt, N., Lassen, B., Ings, S. J., Hsu, D., Hirsch, K. K., & Von Nicolai, C. (2012). Salt tectonics on passive margins: Examples from Santos, Campos and kwanza basins. *Geological Society, London, Special Publications*, *363*(1), 207–244.

Rowan, M. G. (2014). Passive-margin salt basins: Hyperextension, evaporite deposition, and salt tectonics. *Basin Research*, *26*(1), 154–182.

Rowan, M. G. (2020). The South Atlantic and Gulf of Mexico salt basins: Crustal thinning, subsidence and accommodation for salt and presalt strata. *Geological Society, London, Special Publications*, *476*(1), 333–363.

Rowan, M. G., Peel, F. J., & Vendeville, B. C. (2004). Gravity-driven fold-belts on passive margins. In K. R. McClay (Ed.), *Thrust tectonics and hydrocarbon systems*. AAPG Memoir (Vol. *82*, pp. 157–182). American Association of Petroleum Geologists.

Tari, G., Molnar, J., & Ashton, P. (2003). Examples of salt tectonics from West Africa: A comparative approach. *Geological Society, London, Special Publications*, *207*(1), 85–104.

Tari, G., Novotny, B., Jabour, H., & Hafid, M. (2017). Salt tectonics along the Atlantic margin of NW Africa (Morocco and Mauritania). In J. I. Soto, J. Flinch, & G. Tari (Eds.), *Permo-Triassic salt provinces of Europe, North Africa and the Atlantic margins* (pp. 331–351). Elsevier.

Theunissen, T., & Huismans, R. S. (2019). Long-term coupling and feedback between tectonics and surface processes during non-volcanic rifted margin formation. *Journal of Geophysical Research: Solid Earth*, *124*(11), 12323–12347.

Thieulot, C. (2011). FANTOM: Two-and three-dimensional numerical modelling of creeping flows for the solution of geological problems. *Physics of the Earth and Planetary Interiors*, *188*(1–2), 47–68.

Uranga, R. M., Ferrer, O., Zamora, G., Muñoz, J. A., & Rowan, M. G. (2022). Salt tectonics of the offshore Tarfaya Basin, Moroccan Atlantic margin. *Marine and Petroleum Geology*, *138*, 105521.

Wu, Y., Louden, K. E., Funck, T., Jackson, H. R., & Dehler, S. A. (2006). Crustal structure of the Central Nova Scotia margin off eastern Canada. *Geophysical Journal International*, *166*(2), 878–906.

SUPPORTING INFORMATION

Additional supporting information can be found online in the Supporting Information section at the end of this article.

How to cite this article: Pichel, L. M., Huismans, R. S., Gawthorpe, R., & Faleide, J. (2023). How post-salt sediment flux and progradation rate influence salt tectonics on rifted margins: Insights from geodynamic modelling. *Basin Research*, *00*, 1–17. https://doi.org/10.1111/bre.12802